Mathematical Model for the Simulation of Contact-Induced Standing Waves in Tyres by a Rotating Ring Based on Experiment

Ivo Senjanović, Damjan Čakmak, Neven Alujević, Nikola Vladimir, Ivan Ćatipović

University of Zagreb, Faculty of Mechanical Engineering and Naval Architecture, Ivana Lučića 5, 10 002 Zagreb, CROATIA
e-mail: ivo.senjanovic@fsb.hr

SUMMARY

A physics-based mathematical model for the simulation of contact-induced standing waves in rotating tyres is presented. A toroidal balloon mounted on a hub, in contact with a rigid flywheel, is considered. The distance between the hub and the flywheel shafts is kept constant during rotation. The balloon is modelled as a membrane structure, i.e. as a ring on elastic support without flexural stiffness. The differential equations of motion for the ring radial and circumferential displacements are formulated according to the cylindrical shell theory. It is found that the critical rotation speed is a transition parameter from a stable to unstable state, whereas the standing waves denote ring post-buckling behaviour. Boundary conditions at the ring and flywheel contact edges are specified so as to ensure the continuity of ring deformation. The internal load due to the penetration of the flywheel into the expanded ring, as well as the reaction forces in shaft bearings, are determined. The influence of the circumferential displacement on ring response is also analysed. The analytical procedure is verified by comparing the numerical and the available experimental results. In spite of a rather simple balloon model, a good qualitative agreement between the two sets of results is obtained.

KEY WORDS: *rotating tyre; standing waves; ring model; analytical procedure; experiment.*

1.   INTRODUCTION

The generation of standing waves in tyres starts when the tyre rotation speed exceeds a certain critical value. Standing waves are stationary for an observer from the ground. However, an observer located at the tyre periphery rides on the standing waves like a passenger on a ship sailing on sea waves. Hence, the material of a rotating tyre passing through standing waves vibrates and undergoes quite large deformations, dissipating a significant amount of energy in the tyre. Large strains and stresses cause significant fatigue in the tyre material and quick overheating, which may result in tyre failure. Therefore, the critical speed represents a serious performance limitation for tyres of high-speed road vehicles. For traffic

security reasons, the problem of standing waves in tyres has been investigated since the 1950s.

A useful review of early theoretical and experimental work published before 1970 is presented in [1]. Early research on the standing waves phenomenon was mostly theoretical, including both purely analytical and semi-analytical work. Simplified tyre models range from ring substitutions [2-10], to toroidal membrane approximations [11], as well as thin cylindrical [12] and thin toroidal shell simplifications [13]. Ring-based models are a very rough simplification of the real tyre structure. In such models, the tyre belt is typically modelled as a ring, whereas the tyre sidewalls are approximated by distributed radial stiffness. Nowadays, 3D FE models are ordinarily used for the verification of tyre designs, [14-22].

Experimental studies have been predominantly directed to the modal analysis of non-rotating [4], [23-26], and rotating tyres [27]. Dynamic stiffness has been evaluated experimentally on a small-scale tyre [28]. Full-scale tests have been performed to visualise the generation of standing waves and to determine the critical speed of aircraft tyres [29].

It can be seen from the relevant literature that there are many different approaches to modelling tyre dynamic properties. This is particularly the case for the phenomenon of standing waves. They are interpreted in numerous ways: i.e., resulting from a shock at the leading contact edge, in terms of resonance, and as a loss of dynamic stability.

Among a number of published papers, Ref. [7] is interesting since it aims to solve the above dilemmas by looking into the origin of standing wave generation. An experiment was performed in this respect to study the dynamic behaviour of a small inflated balloon tyre mounted above a flywheel while keeping a constant distance between the tyre and the flywheel shafts during the rotation. Experimental observations of standing waves arising beyond a critical speed were presented, including measurements of the spatial profiles of the standing waves. A mathematical model based on a simplified ring model of a toroidal balloon rolling on the ground instead of on the flywheel was developed. The steady-state solutions at any rotation speed were found to be governed by a non-linear boundary value problem. Appropriate boundary conditions were determined using asymptotic arguments and then applied in the numerical calculation. A qualitative correlation analysis showed that the calculated results agree very well with the recorded data.

In spite of the good agreement between the theoretical interpretation of standing waves and the experimental results, the mathematical model presented in Ref. [7] is not fully physics-based. The contact of the ring with the ground instead of with the flywheel is a rather rough simplification with repercussions on the boundary conditions. The mathematical models that have been used in the past are quite intricate and, in some, the theoretical formulations seem to be rather controversial [30]. Therefore, the state of the art in the physical interpretation of the standing waves origin motivates further investigation of this challenging problem.

A new physics-based mathematical model, which models the balloon-flywheel set as a ring in contact with the flywheel, is presented in this paper. The novelty of this model, in comparison to the well-known mathematical model worked out in Ref. [7], widely referred to in the literature and used as a benchmark, can be clarified through several aspects. Firstly, both radial and circumferential displacements are taken into account. The geometric stiffness due to the inflation pressure is employed instead of the "shear stiffness". The shear stiffness is normally not attributable to the balloon, given that it is modelled as a membrane structure in Ref. [7]. This leads to the wrong definition of the critical rotation speed in [7]. In the present mathematical model, the ring rolls on the flywheel as in the experiment and not on the ground

as in [7]. This is very important for a reliable correlation analysis of the calculated and measured results. Boundary conditions are specified in a relatively simple way as a linear problem, while this task is solved in [7] in a rather complicated manner. In the new mathematical model, the experimental standing wave profiles and the ripple at the balloon-flywheel leading contact edge are successfully captured compared to those simulated in [7]. In addition, the internal loads and the bearing reaction forces are determined.

This paper is structured into 14 sections. In this first introductory section, the state of the art in the field of standing waves phenomenon is summarized and the motivation for the present work is pointed out. In the second section, an observation on the related experiment is made. The mathematical model for the ring-flywheel system is worked out in the third section. Sections 4 and 5 deal with the solution of differential equations and boundary conditions, respectively. The ripple theory near the leading contact edge is formulated in Section 6. Internal loads and bearing reaction forces are analysed in Section 7. A simplified mathematical model ignoring circumferential displacement as a small quantity is presented in Section 8. The critical rotation speed is analysed in Section 9. Section 10 is concerned with an illustrative numerical example. Section 11 is dedicated to qualitative correlation analysis of the theoretical and experimental results. In section 12 an improvement of the mathematical model based on the experimental results is presented. Section 13 includes a discussion while conclusions are drawn in Section 14.

2. OBSERVATION ON THE RELATED EXPERIMENT

As mentioned in the Introduction, an experimental and theoretical study of standing waves of a small rotating toroidal balloon is described in [7]. The balloon is mounted on a hub which is driven by an electromotor. The pressurized balloon makes contact with a solid aluminium flywheel and the distance between their shafts is fixed during the testing, Figure 1a. The penetration of the flywheel into the balloon progressively grows as the rotation speed increases.

The balloon is a membrane structure with very small bending stiffness. Hence, its free surface is only locally deformed at the contact edges up to a critical speed, Ω_c. If this ripple is ignored, there is a discontinuity of the balloon generatrix slope at point P in Figure 1b. By increasing the rotation speed Ω over Ω_c, standing waves are generated on the trailing contact side, Figure 1b. The balloon undergoes significant deformation before failure. However, despite the large deformations involved, the displacements of the balloon crown remain predominantly radial. This is noticed by observing the marked radial line on the balloon during the increase of the rotation speed.

The described standing waves phenomenon is similar to the generation of a ship's wake waves behind the stern during a voyage on a calm sea. This analogy is illustrated in Figure 2. The penetration area of the flywheel into the rotating balloon (intersection) is analogous to the submerged part of the ship. The wavelengths and amplitudes of the standing waves and the wake waves depend on the flywheel angular velocity and the ship speed, respectively. In both examples, a ripple is generated at the leading contact edge.
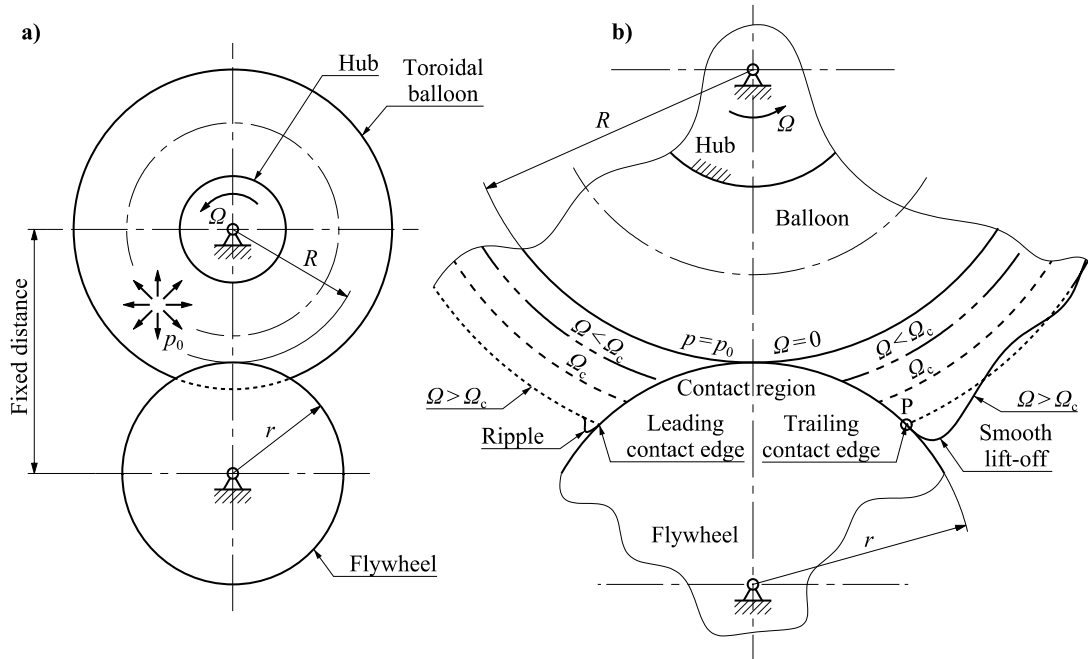
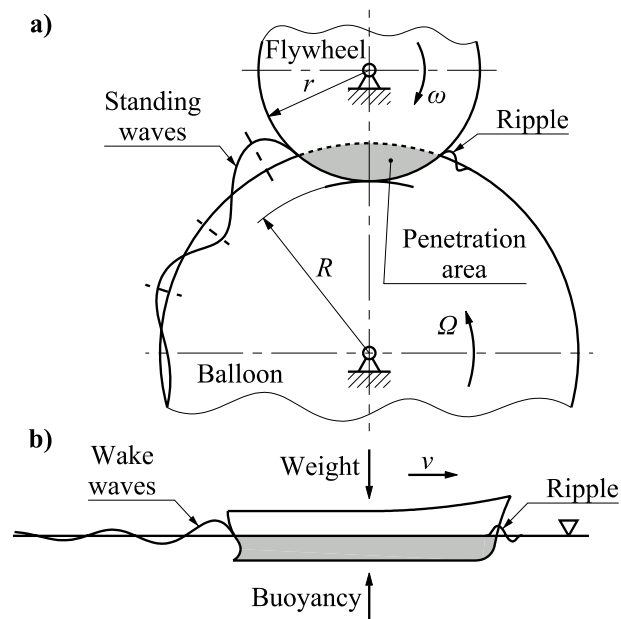**Fig. 1** *Experimental set-up and balloon deformation (according to [7])*

Fig. 2 *Analogy between the generation of ring standing waves and ship wake waves*

The shape of the standing waves is sinusoidal with a logarithmically decreasing amplitude. In order to investigate the standing wave phenomenon qualitatively, the balloon can be conceived as a rotating ring with equivalent particulars. The bending stiffness of the balloon shell is very small and can be ignored in the mathematical model.

3. MATHEMATICAL MODEL

The toroidal balloon in the experiment is a pressurized membrane structure exposed to a centrifugal load. This results in a large deflection and a small stretch. The same behaviour has to be captured in the ring model of the balloon, Figure 3. A complete set of two coupled differential equations for the ring motion with radial, w, and circumferential, v, displacements, Figure 3c, can be deduced from the cylindrical shell theory [31] and [32]. These equations can be written in a symbolic form as:

$$F_{11}\big(w(\psi)\big) - F_{12}\big(v(\psi)\big) = q_r$$
$$-F_{21}\big(w(\psi)\big) + F_{22}\big(v(\psi)\big) = -q_c, \tag{1}$$

where:

$$F_{11}\big(w(\psi)\big) = \frac{D}{R^4}\frac{\partial^4 w}{\partial\psi^4} - \frac{N_\psi}{R^2}\frac{\partial^2 w}{\partial\psi^2} + \left(\frac{K+N_\psi}{R^2} + k_r - m\Omega^2\right)w + m\frac{\partial^2 w}{\partial t^2}$$

$$F_{12}\big(v(\psi)\big) = \frac{D}{R^4}\frac{\partial^3 v}{\partial\psi^3} - \frac{1}{R^2}\big(K+2N_\psi\big)\frac{\partial v}{\partial\psi} + 2m\Omega\frac{\partial v}{\partial t}$$

$$F_{21}\big(w(\psi)\big) = \frac{D}{R^4}\frac{\partial^3 w}{\partial\psi^3} - \frac{1}{R^2}\big(K+2N_\psi\big)\frac{\partial w}{\partial\psi} + 2m\Omega\frac{\partial w}{\partial t}$$

$$F_{22}\big(v(\psi)\big) = -\frac{1}{R^2}\left(\frac{D}{R^2} + K + N_\psi\right)\frac{\partial^2 v}{\partial\psi^2} + \left(\frac{N_\psi}{R^2} + k_c - m\Omega^2\right)v + m\frac{\partial^2 v}{\partial t^2}. \tag{2}$$
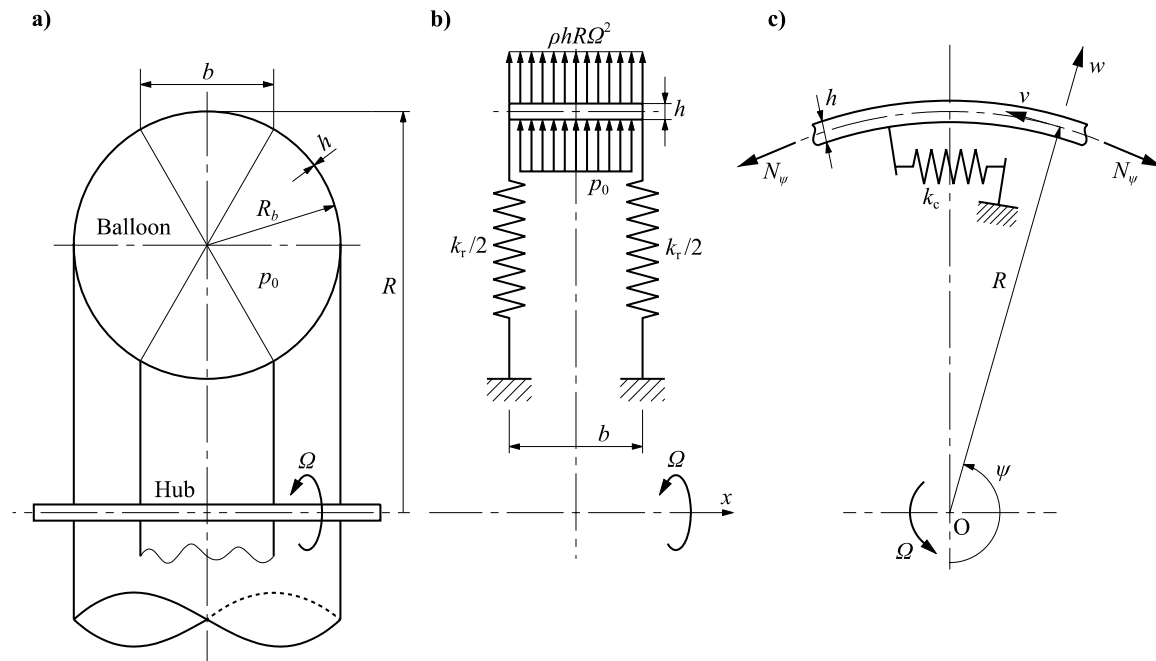

Fig. 3 *Toroidal balloon and the corresponding ring model*

It can be seen that the differential operators in functions $F_{12}(v(\psi))$ and $F_{21}(w(\psi))$ are identical.

In Eqs. (2) the symbols have the following meaning:

R – ring radius

ψ – position angle

D – bending stiffness

K – tensional stiffness

k_r – radial stiffness of elastic foundation

k_c – circumferential stiffness of elastic foundation

m – distributed mass per unit length

Ω – ring rotation speed

N_ψ – membrane force.

Symbols k_r and k_c represent the equivalent tensional and shear stiffness of the balloon side-shell, respectively.

In the considered case, the radial load in Eqs. (1) consists of two parts, i.e.:

$$q_r = q + mR\Omega^2, \quad q = bp, \tag{3}$$

where the first term is the distributed load due to the inflation pressure, p, acting on the breadth of the ring cross-section, b, Figure 3b, while the second term is the centrifugal load. Due to the inflation pressure, the cross-section of the balloon is expanded, whereas the centrifugal load causes pseudo-elliptical deformation of the cross-section, as in the case of a toroidal shell, Figure 4, [33]. The circumferential load q_c in Eqs. (1) is zero in the considered case.
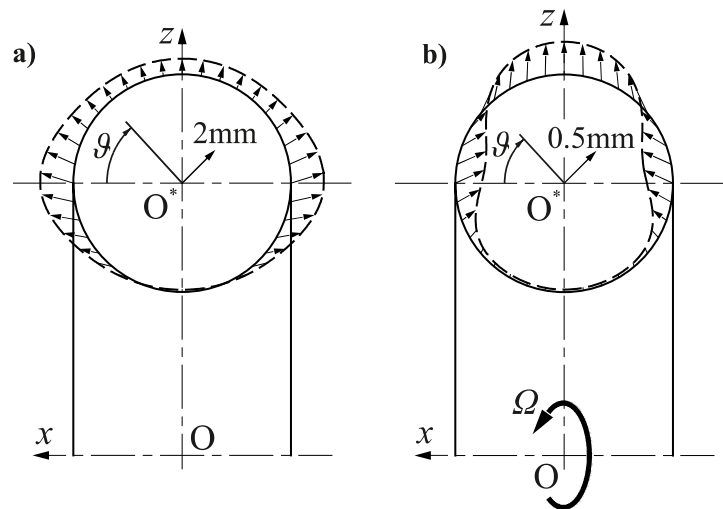
Fig. 4 *Toroidal shell cross-section deformation due to a) internal pressure and b) centrifugal load, [33], (with indicated scale)*

Tyres are ordinarily pressurized in order to increase their stiffness which is realized through geometric stiffness. The pressure load increases the ring radius and induces a membrane force:

$$N_\psi = N_p = Rq. \tag{4}$$

This pre-stressed state is used as a referent for the vibration analysis, and the pressure load is accordingly excluded from Eqs. (2). The ring bending stiffness is also very small and can be omitted. Hence, the rearranged differential Eqs. (1) and (2) take the form:

$$-\frac{q}{R}\frac{\partial^2 w}{\partial \psi^2} + \left(\frac{K}{R^2} + \frac{q}{R} + k_r - m\Omega^2\right)w + m\frac{\partial^2 w}{\partial t^2} + \frac{1}{R^2}(K+2Rq)\frac{\partial v}{\partial \psi} - 2m\Omega\frac{\partial v}{\partial t} = mR\Omega^2, \tag{5}$$

$$-\left(\frac{K}{R^2} + \frac{q}{R}\right)\frac{\partial^2 v}{\partial \psi^2} + \left(\frac{q}{R} + k_c - m\Omega^2\right)v + m\frac{\partial^2 v}{\partial t^2} + \frac{1}{R^2}(K+2Rq)\frac{\partial w}{\partial \psi} - 2m\Omega\frac{\partial w}{\partial t} = 0, \tag{6}$$

where R is now the radius of the pressurized ring.

Equations (5) and (6) are written with reference to a rotating coordinate system fixed to the rotating ring. For a ground-fixed coordinate system, a new variable must be introduced:

$$\varphi = \Omega t + \psi. \tag{7}$$

Transformation of the coordinate system and the assumption that displacements are stationary in the ground-fixed frame lead to the following relationships which are also valid for v:

$$\frac{\partial^n w}{\partial \psi^n} = \frac{d^n w}{d\varphi^n}, \quad \frac{\partial^n w}{\partial t^n} = \Omega^n \frac{d^n w}{d\varphi^n}. \tag{8}$$

Substituting Eqs. (8) into Eqs. (5) and (6) yields ordinary differential equations for the description of standing waves:

$$\left(m\Omega^2 - \frac{q}{R}\right)\frac{d^2 w}{d\varphi^2} + \left(\frac{K}{R^2} + k_r + \frac{q}{R} - m\Omega^2\right)w + \left(\frac{K}{R^2} + 2\frac{q}{R} - 2m\Omega^2\right)\frac{dv}{d\varphi} = mR\Omega^2, \tag{9}$$

$$-\left(\frac{K}{R^2} + \frac{q}{R} - m\Omega^2\right)\frac{\partial^2 v}{\partial \varphi^2} + \left(\frac{q}{R} + k_c - m\Omega^2\right)v + \left(\frac{K}{R^2} + 2\frac{q}{R} - 2m\Omega^2\right)\frac{\partial w}{\partial \varphi} = 0. \tag{10}$$

Equations. (9) and (10) are time-independent in the ground-fixed coordinate system, which is a characteristic feature of standing waves.

During the experiment, a ripple is observed at the leading contact edge of the balloon and the flywheel, Figure 1. It is caused by deformation discontinuity. This is a very short local bending and in the ring model it may be considered as a beam bending on elastic foundation. The corresponding differential equation may be formulated according to Eqs. (1) and (2):

$$\frac{D}{R^4}\frac{d^4 w}{d\varphi^4} + \left(\frac{K}{R^2} + k_r + \frac{q}{R} - m\Omega^2\right)w = 0. \tag{11}$$

Also, a smooth lift-off of the standing waves at the trailing contact edge is recorded like a ripple. These local bending and standing waves are two different problems of a different order of magnitude. Therefore, they can be decomposed due to their small coupling which is ordinarily done in the perturbation method. The differential equation for local bending is extracted from Eqs. (1) and (2) in the same form as Eq. (11).

4. SOLUTION OF THE DIFFERENTIAL EQUATIONS FOR STANDING WAVES

Particular solutions of Eqs. (9) and (10) are $w_p = w_0$, $v_p = 0$, where:

$$w_0 = \frac{mR\Omega^2}{\dfrac{K}{R^2} + k_r + \dfrac{q}{R} - m\Omega^2} \tag{12}$$

is the membrane radial displacement. Homogeneous solutions can be assumed in the exponential form:

$$w = Ae^{r\varphi}, \quad v = Be^{r\varphi}. \tag{13}$$

Substituting Eqs. (13) into Eqs. (9) and (10) yields:

$$\begin{bmatrix} a_{11} & a_{12} \\ a_{21} & a_{22} \end{bmatrix} \begin{Bmatrix} A \\ B \end{Bmatrix} = \{0\}, \tag{14}$$

Where:

$$a_{11} = dr^2 + \left(\frac{K}{R^2} + k_r - d \right)$$

$$a_{12} = a_{21} = \left(\frac{K}{R^2} - 2d \right) r \tag{15}$$

$$a_{22} = \left(d - \frac{K}{R^2} \right) r^2 + k_c - d.$$

and

$$d = m\Omega^2 - \frac{q}{R}. \tag{16}$$

The roots of Eq. (14) are obtained from condition $\text{Det}(r) = 0$, which leads to the characteristic equation:

$$ar^4 + br^2 + c = 0, \tag{17}$$

where:

$$a = d \left(d - \frac{K}{R^2} \right)$$

$$b = \left(2\frac{K}{R^2} + k_c - 4d \right) \left(d - \frac{K}{R^2} \right) + d(k_c - 2d) \tag{18}$$

$$c = \left(\frac{K}{R^2} + k_r - d \right) (k_c - d).$$

Four solutions of Eq. (17) read:

$$r_j = \pm \sqrt{\frac{-b \pm \sqrt{b^2 - 4ac}}{2a}}, \quad j = 1,2,3,4. \tag{19}$$

For the case $d = 0$, Eq. (16), the variable a, as given by the first of Eqs. (18), is also zero. Consequently, one finds only two roots of Eq. (17), i.e.:

$$r_{1,2} = \pm\alpha, \quad \alpha = \sqrt{\frac{\left(\dfrac{K}{R^2} + k_r\right)k_c}{\left(2\dfrac{K}{R^2} + k_c\right)\dfrac{K}{R^2}}}. \tag{20}$$

Since both roots are real, the corresponding exponential displacement functions cannot describe standing waves.

If $d < 0$, Eq. (19) yields four real roots:

$$r_j = \pm(\alpha \pm \beta), \quad j = 1,2,3,4. \tag{21}$$

This solution is also not applicable for the analysis of standing waves.

If $d > 0$, two roots are real and two are imaginary:

$$r_j = \pm\begin{Bmatrix} \pm\alpha \\ \pm i\beta \end{Bmatrix}, \quad j = 1,2,3,4. \tag{22}$$

In this case, solutions of Eqs. (9) and (10) are complex:

$$\tilde{w} = \tilde{A}_1 e^{\alpha\varphi} + \tilde{A}_2 e^{-\alpha\varphi} + \tilde{A}_3 e^{i\beta\varphi} + \tilde{A}_4 e^{-i\beta\varphi} + w_0, \tag{23}$$

$$\tilde{v} = \tilde{B}_1 e^{\alpha\varphi} + \tilde{B}_2 e^{-\alpha\varphi} + \tilde{B}_3 e^{i\beta\varphi} + \tilde{B}_4 e^{-i\beta\varphi}. \tag{24}$$

The integration constants $\tilde{A}_i$ and $\tilde{B}_i$ are linked via Eq. (14):

$$\tilde{B}_j = -\frac{a_{11}(r_j)}{a_{12}(r_j)}\tilde{A}_j = -\frac{a_{21}(r_j)}{a_{22}(r_j)}\tilde{A}_j, \quad j = 1,2,3,4. \tag{25}$$

The second relation of Eq. (25) is more practical and by employing Eqs. (15) and (22) one obtains for a particular pairs of constants:

$$\begin{aligned} \tilde{B}_1 &= -\varepsilon_1\tilde{A}_1, \quad \tilde{B}_2 = \varepsilon_2\tilde{A}_2, \\ \tilde{B}_3 &= -i\varepsilon_3\tilde{A}_3, \quad \tilde{B}_4 = i\varepsilon_4\tilde{A}_4, \end{aligned} \tag{26}$$

where:

$$\varepsilon_1 = \varepsilon_2 = \frac{\left(\dfrac{K}{R^2} - 2d\right)\alpha}{\left(d - \dfrac{K}{R^2}\right)\alpha^2 + k_c - d},$$

$$\varepsilon_3 = \frac{\left(\dfrac{K}{R^2} - 2d\right)\beta}{-\left(d - \dfrac{K}{R^2}\right)\beta^2 + k_c - d}, \tag{27}$$

$$\varepsilon_4 = \frac{\left(\dfrac{K}{R^2} - 2d\right)\beta}{\left(d - \dfrac{K}{R^2}\right)\beta^2 + k_c - d},$$

Actual ring displacements are real parts of the complex solutions (23) and (24), i.e. $w = Re(\tilde{w})$ and $v = Re(\tilde{v})$. Setting:

$$\tilde{A}_j = A_j^0 + i A_j^*,$$
$$e^{\pm i\beta\varphi} = cos(\beta\varphi) \pm i\,sin(\beta\varphi) \tag{28}$$

one finds from (23) and (24):

$$w = A_1^0 e^{\alpha\varphi} + A_2^0 e^{-\alpha\varphi} + \left(A_3^0 + A_4^0\right)cos(\beta\varphi) + \left(-A_3^* + A_4^*\right)sin(\beta\varphi) + w_0. \tag{29}$$

Furthermore, by employing relations, (26) yields from (24):

$$v = -\varepsilon_1 A_1^0 e^{\alpha\varphi} + \varepsilon_2 A_2^0 e^{-\alpha\varphi} + \left(\varepsilon_3 A_3^0 + \varepsilon_4 A_4^0\right)sin(\beta\varphi) + \left(\varepsilon_3 A_3^* - \varepsilon_4 A_4^*\right)cos(\beta\varphi). \tag{30}$$

The ring displacements, Eqs. (29) and (30), are expressed in terms of six integration constants.

In the numerical example for standing waves simulation in the considered balloon by the ring model, the circumferential stiffness k_c in the denominator of factors ε_j, Eqs. (27), is predominant. As a result $\varepsilon_3 \approx \varepsilon_4$ and the number of integration constants in Eqs. (29) and (30) is reduced to four:

$$w = A_1 e^{\alpha\varphi} + A_2 e^{-\alpha\varphi} + A_3\,cos(\beta\varphi) + A_4\,sin(\beta\varphi) + w_0. \tag{31}$$

$$v = -\varepsilon_1 A_1 e^{\alpha\varphi} + \varepsilon_1 A_2 e^{-\alpha\varphi} + \varepsilon_3 A_3\,sin(\beta\varphi) - \varepsilon_3 A_4\,cos(\beta\varphi). \tag{32}$$

The ring rotation speed, which characterizes the transition of response from the exponential to the sine/cosine shape at $d = 0$, Eq. (16), is the critical speed:

$$\Omega_c = \sqrt{\frac{q}{mR}}. \tag{33}$$
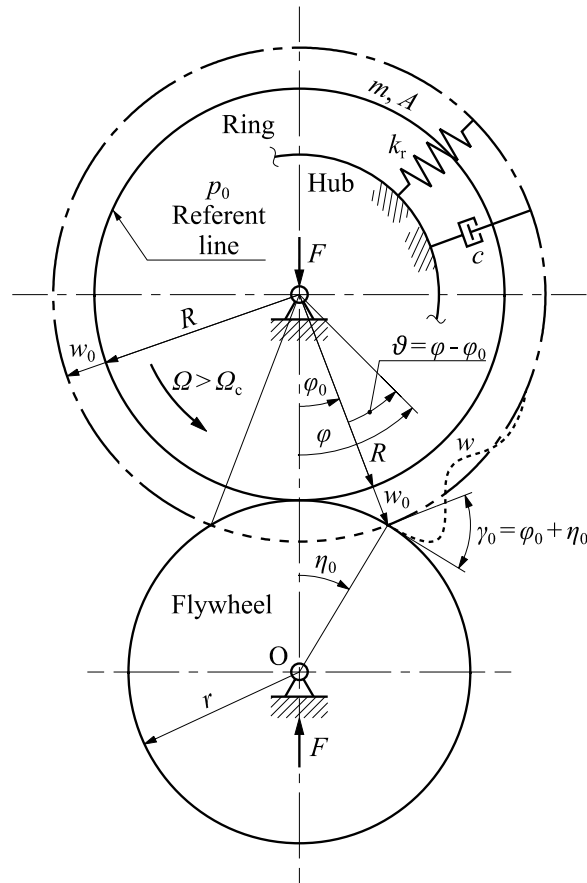
5. BOUNDARY CONDITIONS AND THE DISCONTINUITY ANGLE

The ring and flywheel particulars are shown in Figure 5. For simplicity, a new variable $\vartheta = \varphi - \varphi_0$, measured from the trailing contact edge, is introduced. The argument in Eqs. (31) and (32) is changed accordingly. Since the standing waves are harmonic, one can write:

$$w = A_3\,cos(\beta\vartheta) + A_4\,sin(\beta\vartheta) + w_0, \tag{34}$$

$$v = \varepsilon_3 A_3\,sin(\beta\vartheta) - \varepsilon_3 A_4\,cos(\beta\vartheta). \tag{35}$$

The boundary conditions are specified for displacement w, Eq. (34), and the rotation angle:

$$\beta_{rot} = \frac{1}{R}\left(v - \frac{dw}{d\vartheta}\right) = \frac{1}{R}\left[\varepsilon_3 A_3\,sin(\beta\vartheta) - \varepsilon_3 A_4\,cos(\beta\vartheta) + A_3\beta\,sin(\beta\vartheta) - A_4\beta\,cos(\beta\vartheta)\right] \tag{36}$$

Fig. 5 *Ring and flywheel particulars and displacements at the trailing contact edge, w_0 and γ_0*

A ring mass particle, leaving the trailing contact edge, tends to move continuously in the tangential direction of flywheel, Figure 6. However, the radial spring causes its oscillation around the circle of membrane expansion with radius $R + w_0$. The trailing contact edge is obviously the inflection point of the mass trajectory, and boundary conditions for standing waves read:

$$\vartheta = 0: \quad w(0) = w_0, \quad \beta_{rot}(0) = -\gamma_0, \tag{37}$$

where γ_0 is the discontinuity angle, Figure 6. By satisfying Eqs. (37) yields:
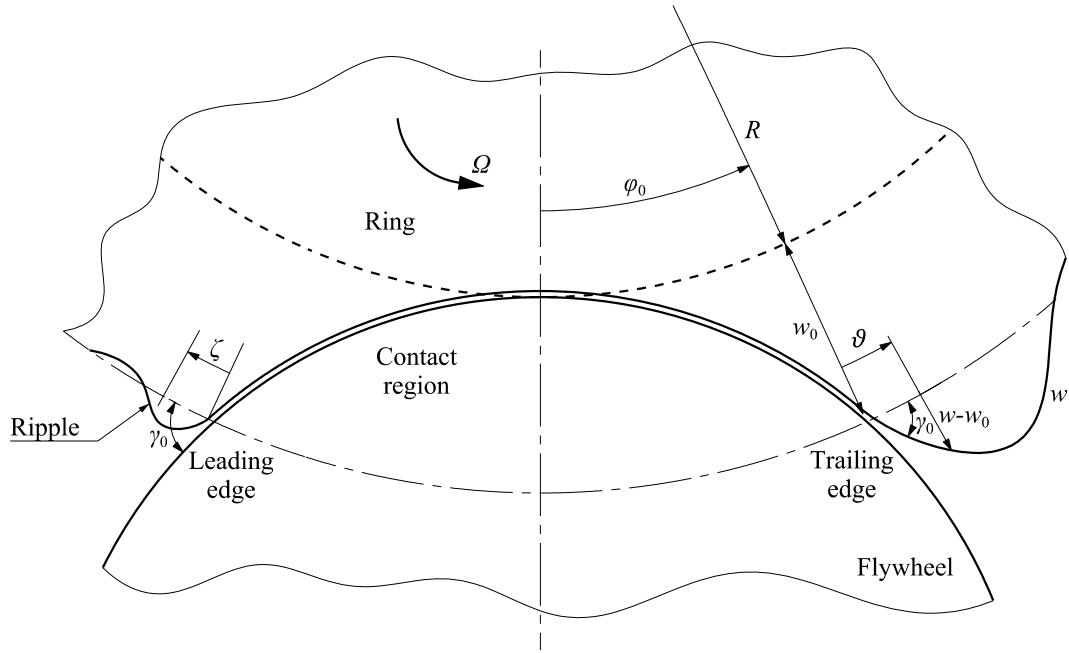
$$A_3 = 0, \quad A_4 = \frac{R\gamma_0}{\beta + \varepsilon_3} \tag{38}$$

As a result the ring displacements read:

$$w = \frac{R\gamma_0}{\beta + \varepsilon_3} \sin(\beta\vartheta) + w_0, \tag{39}$$

$$v = -\frac{\varepsilon_3 R\gamma_0}{\beta + \varepsilon_3} \cos(\beta\vartheta). \tag{40}$$

It is obvious that w and v are moved in phase for $\pi/2$.

Fig. 6 *Boundary conditions at contact edges*

Let us now determine the discontinuity angle $\gamma_0 = \varphi_0 + \eta_0$. According to Figure 7, angles φ_0 and η_0 both depend on the deflection w_0, and the following relationships in the vertical and horizontal direction, respectively, can be specified for their determination:

$$\left(R + w_0\right)\cos\varphi_0 + r\cos\eta_0 = R + r,$$ **(41)**

$$\left(R + w_0\right)\sin\varphi_0 = r\sin\eta_0,$$ **(42)**

where r is the radius of the flywheel. By employing the basic trigonometric identity $\sin^2\alpha + \cos^2\alpha = 1$, variable φ_0, as well as variable η_0, can be eliminated from (41) and (42), respectively. As a result, one obtains:

$$\cos\eta_0 = 1 - \frac{\left(2R + w_0\right)w_0}{2\left(R + r\right)r}.$$ **(43)**

$$\cos\varphi_0 = \frac{2\left(R + r\right)R + \left(2R + w_0\right)w_0}{2\left(R + r\right)\left(R + w_0\right)},$$ **(44)**

where w_0 is specified by Eq. (12). If $w_0 = 0$, both angles $\eta_0 = \varphi_0 = 0$. It can be seen that the boundary value problem is linear.
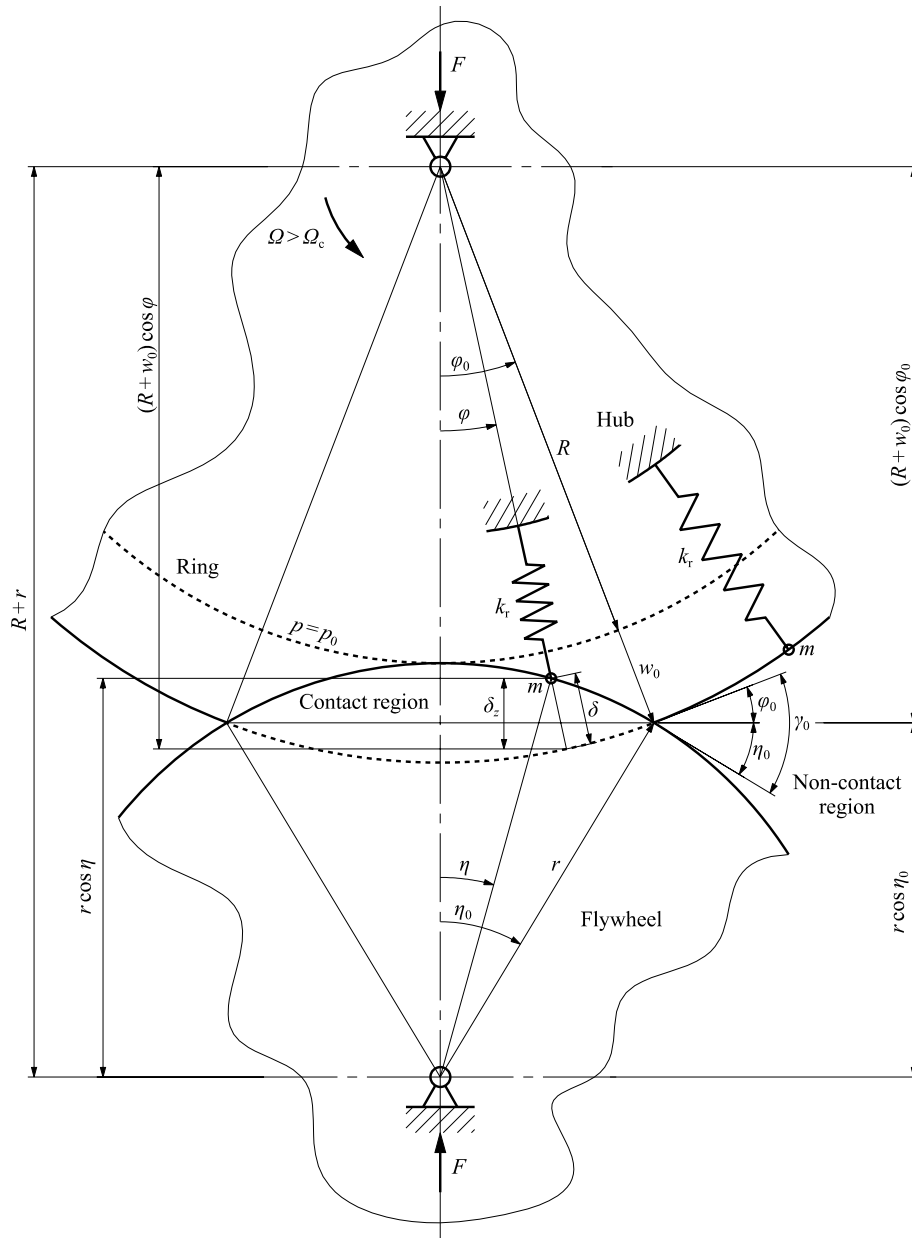
Fig. 7 *Determination of edge discontinuity angle, γ_0, and bearing reaction forces, F*

6. RIPPLES NEAR THE CONTACT EDGES

Ripples, Figure 6, are described by differential Eq. (11) as a local bending phenomenon. Assuming the solution of Eq. (11) in the exponential form $w = Ae^{r\varphi}$, one obtains the characteristic equation:

$$\frac{D}{R^4}r^4 + \tilde{k} = 0, \tag{45}$$

where:

$$\tilde{k} = \frac{K}{R^2} + k_r + \frac{q}{R} - m\Omega^2 \tag{46}$$

is dynamic stiffness. The solution of (45) reads:

$$r_{1-4} = \pm(1 \pm i)\lambda, \tag{47}$$

where:

$$\lambda = \sqrt[4]{\frac{R^4 \tilde{k}}{4D}}. \tag{48}$$

The solution of the governing Eq. (11) can be presented in the form:

$$w = A_1 e^{\lambda\varphi} sin(\lambda\varphi) + A_2 e^{\lambda\varphi} cos(\lambda\varphi) + A_3 e^{-\lambda\varphi} sin(\lambda\varphi) + A_4 e^{-\lambda\varphi} cos(\lambda\varphi). \tag{49}$$

Since ripple is a local boundary disturbance, there is no mutual interference between the two contact edges. Hence, only the two decaying terms in Eq. (49) are relevant. By introducing the new coordinate, measured from the leading contact edge, Figure 6, one can write:

$$w = A e^{-\lambda\zeta} sin(\lambda\zeta) + B e^{-\lambda\zeta} cos(\lambda\zeta). \tag{50}$$

Satisfying boundary conditions $w(0) = 0$ and $\beta_{rot}(0) = -\gamma_0$, yields:

$$w = R\frac{\gamma_0}{\lambda} e^{-\lambda\zeta} sin(\lambda\zeta). \tag{51}$$

The value of parameter λ, Eq. (48), is quite large, giving a small wavelength compared to the wave number of standing waves β, Section 4, and a rapid decrease of the wave amplitude with respect to an ordinary damping coefficient. The ripple amplitude depends on the ring rotation speed via γ_0, i.e., w_0, Eq. (12).

7. INTERNAL LOADS AND BEARING REACTION FORCES

In the non-contact region, the rotation induced centrifugal load is in equilibrium with the ring reaction, Figure 7. This follows from Eq. (9) for constant displacements:

$$k_t w_0 = m(R + w_0)\Omega^2, \tag{52}$$

where:

$$k_t = \frac{K}{R^2} + k_r + \frac{q}{R} \tag{53}$$

is the total radial stiffness.

On the other hand, in the contact region this equilibrium is disturbed due to the penetration of the flywheel into the ring, δ, Figure 7. This causes an internal expansion load which is transmitted to the ring and flywheel bearings, Figure 7:

$$q_b = k_r \delta, \tag{54}$$

where k_r is the radial spring stiffness.

The reaction force in the bearings equals the integral of the load vertical component over the contact region:

$$F = 2\int_0^{\varphi_0} q_b\left(R+w_0\right)\cos\varphi\,d\varphi. \tag{55}$$

By employing Eq. (54), one obtains:

$$F = 2k_r\left(R+w_0\right)\int_0^{\varphi_0} \delta\cos\varphi\,d\varphi. \tag{56}$$

In order to determine the bearing reaction force, it is necessary to define the flywheel penetration depth into the ring, δ. According to Figure 7, one can write for the penetration depth:

$$\delta = \frac{1}{\cos\varphi}\left[\left(R+w_0\right)\cos\varphi + r\cos\eta - \left(R+r\right)\right]. \tag{57}$$

The aim here is to express δ as a function of only one variable for subsequent integration. It is natural to use angle φ as a unique variable. From Figure 7, it is seen that:

$$\left(R+w_0-\delta\right)\sin\varphi = r\sin\eta. \tag{58}$$

Variable η can be eliminated from Eqs. (57) and (58) by employing the basic trigonometric identity $\sin^2\eta + \cos^2\eta = 1$. This leads to the quadratic algebraic equation:

$$x^2 - 2bx\cos\varphi + b^2 - 1 = 0, \tag{59}$$

where:

$$x = \frac{R+w_0-\delta}{r}, \quad b = \frac{R+r}{r}. \tag{60}$$

By solving Eq. (59), one finds:

$$\delta = R + w_0 - \left(R+r\right)\cos\varphi + r\sqrt{1 - \left(\frac{R+r}{r}\right)^2 \sin^2\varphi}. \tag{61}$$

At $\varphi = 0$, it can be seen that $\delta = w_0$, as shown in Figure 7.

Finally, by substituting (61) into (56) and integrating, one obtains for the bearing reaction force:

$$F = k_r\left(R+w_0\right)\left\{ \begin{array}{c} 2\left(R+w_0\right)\sin\varphi_0 - \left(R+r\right)\left(\varphi_0 + \sin\varphi_0\cos\varphi_0\right) + \\ r\left[\sin\varphi_0\sqrt{1-\left(\frac{R+r}{r}\right)^2\sin^2\varphi_0} + \frac{r}{R+r}arcsin\left(\frac{R+r}{r}\sin\varphi_0\right)\right] \end{array} \right\}. \tag{62}$$

8. SIMPLIFIED MATHEMATICAL MODEL WITH INCORPORATED DAMPING

In the numerical example for simulation of the recorded balloon standing waves, it is found that all coefficients ε_j, Eqs. (27), in the expression for ring circumferential displacements v, Eq. (30), are of 10^{-3} order. Therefore, v can be ignored in the system of differential Eqs. (9) and

(10). The governing differential equation for radial displacement with incorporated viscous damping force reads:

$$\left(m\Omega^2 - \frac{q}{R}\right)\frac{d^2 w}{d\varphi^2} + c\Omega\frac{dw}{d\varphi} + \left(\frac{K}{R^2} + k_r + \frac{q}{R} - m\Omega^2\right)w = mR\Omega^2, \tag{63}$$

where c is the damping coefficient. The particular solution of Eq. (63), w_0, is the same as in the sophisticated mathematical model, Eq. (12). The roots of the characteristic equation of differential Eq. (63) are:

$$r_{1,2} = -\mu \pm i\beta. \tag{64}$$

where:

$$\mu = \frac{c\Omega}{2\left(m\Omega^2 - \frac{q}{R}\right)}, \tag{65}$$

$$\beta = \frac{\sqrt{4\left(m\Omega^2 - \frac{q}{R}\right)\left(\frac{K}{R^2} + k_r + \frac{q}{R} - m\Omega^2\right) - c^2\Omega^2}}{2\left(m\Omega^2 - \frac{q}{R}\right)}. \tag{66}$$

Ignoring the damping term, as a very small quantity yields:

$$\beta = \sqrt{\frac{\frac{K}{R^2} + k_r + \frac{q}{R} - m\Omega^2}{m\Omega^2 - \frac{q}{R}}}. \tag{67}$$

The denominator in Eq. (67) is positive if $\Omega > \Omega_c$, where the critical rotation speed is the same as in the sophisticated mathematical model, Eq. (33). In that case, the radial displacement in the shifted coordinate system $\vartheta = \varphi - \varphi_0$, Figure 5, reads:

$$w = A_1 e^{-\mu\vartheta} \sin(\beta\vartheta) + A_2 e^{-\mu\vartheta} \cos(\beta\vartheta) + w_0. \tag{68}$$

Satisfying the boundary conditions as explained in Section 5, one obtains:

$$w = \frac{R\gamma_0}{\beta} e^{-\mu\vartheta} \sin(\beta\vartheta) + w_0. \tag{69}$$

A direct relationship is possible between the wave number β and the membrane radial displacement w_0. If the common terms from the corresponding Eqs. (12) and (67) are eliminated, the following is obtained:

$$\beta = \sqrt{\frac{mR\Omega^2}{\left(m\Omega^2 - \frac{q}{R}\right)w_0}}. \tag{70}$$

It is obvious that if $\Omega = \Omega_c$, the number of standing waves $\beta = \infty$, while their amplitude, Eq. (69), equals zero.

9. CRITICAL ROTATION SPEED AND GENERATION OF STANDING WAVES

Following the theoretical considerations in Section 4, one can give a definition of the critical rotation speed and explain the origin of the generation of standing waves.

The critical speed is a value of the rotation speed at which the compressive membrane force, $N_\Omega = mR^2\Omega^2$, induced by the moving mass, overcomes the tensional pressure membrane force, $N_p = Rbp$, Figure 8. Hence, one finds:

$$\Omega_c = \sqrt{\frac{bp}{mR}}. \tag{71}$$
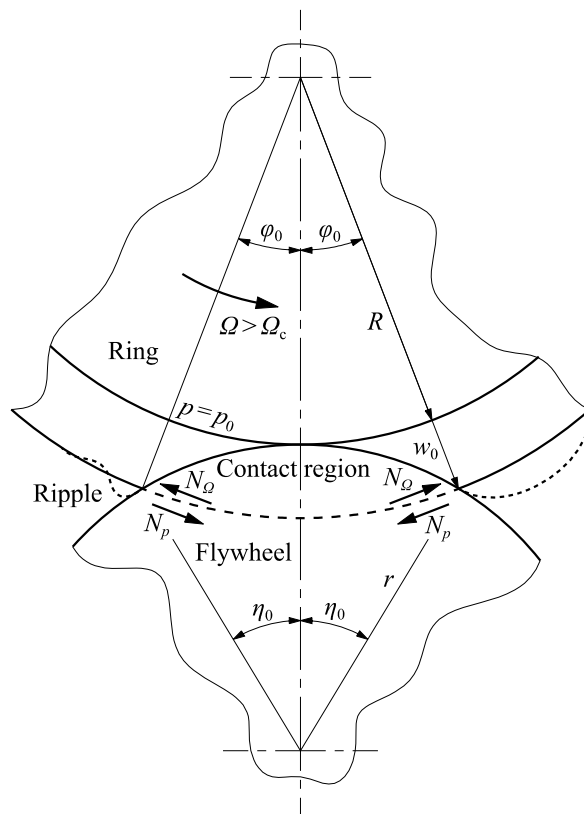
Fig. 8 *Moving-mass-induced membrane force, N_Ω, and inflation pressure membrane force, N_p, and generation of standing waves*

The resulting compressive force, $N = N_p - N_\Omega$, acts all over the ring circumference from the leading to the trailing contact edge. The ring is relaxed since, being a membrane structure, it is unable to withstand such a force. As a result, standing waves are initiated. By increasing the rotation speed, their amplitude and length are progressively increased. If there is no damping, the standing waves are distributed all over the ring between the contact edges, having the same profile. However, if damping is involved, it causes a decay of the standing waves amplitude envelopes, so that they would normally vanish before the leading contact edge. A significant increase in the rotation speed leads to higher pressure, heating, large deformation, fatigue and finally ring collapse.

The origin of standing waves generation is a loss of ring stability. This is not buckling in the classical sense when a structure loses its stability due to an increase of the geometric stiffness over the bending stiffness. In the case of standing waves, buckling occurs when geometric

stiffness due to rotating mass overcomes the geometric stiffness of the inflation pressure. Ring collapse is not instantaneous. The development of standing waves is actually post-buckling behaviour.

10. ILLUSTRATIVE NUMERICAL EXAMPLE ADAPTED TO THE EXPERIMENTAL SET-UP

RING AND FLYWHEEL DATA

In order to evaluate the proposed mathematical model for the simulation of standing waves, the following parameters of the ring-flywheel system are used, Figures 3 and 5:

$R = 0.06$ m, $r = 0.05$ m, $b = 0.025$ m, $h = 0.002$ m, $E = 1 \cdot 10^6$ N/m^2, $\rho = 1100$ kg/m^3, $p_0 = 13.5$ kN/m^2, $k_r = k_c = 2.448 \cdot 10^4$ N/m^2, $\mu = 0.3$ (empirical).

The values of the two radii are close to those from the experiment [7]. Parameter p_0 is the initial inflation pressure. R is the radius of the pressurized ring, which is in contact with the flywheel at the beginning of the experiment.

Based on the given data, some additional parameters are determined:

ring cross-sectional area: $A = bh = 5 \cdot 10^{-5}$ m^2

tensile stiffness: $K = EA = 50$ N

mass per unit length: $m = \rho A = 0.055$ kg/m

pressure load per unit breadth: $q_0 = p_0 b = 337.5$ N/m

critical rotation speed, Eq. (33): $\Omega_c = 320$ rad/s $= 51$ Hz $= 3054$ rpm

membrane radial displacement at Ω_c, Eq. (12): $w_0^c = 0.0088$ m.

APPLICATION OF THE SIMPLIFIED MATHEMATICAL MODEL

A ring rotation speed of $\Omega = 400$ rad/s is chosen for the analysis of the generation of standing waves. This value is close to the maximum speed used in the experiment, [7]. The speed ratio is $\Omega/\Omega_c = 1.25$. For the prescribed rotation speed, one obtains the corresponding membrane radial displacement from Eq. (12), $w_0 = 0.015$ m.

The wave number can be determined by employing Eq. (70), giving $\beta = 3.33$. This is a rather small number of standing waves for correlation analysis with the recorded wave profile. It is difficult to simulate the non-linear dynamic behaviour of a 3D balloon in a quantitative sense by a simple ring model in each aspect. Therefore, in this qualitative analysis, $\beta = 8$ is chosen according to the experimental results for the maximum rotation speed, $\Omega = 420$ rad/s, before the balloon failure, [7]. This implies an increase in the inflation pressure up to 19.8 kN/m^2 according to Eq. (70).

Boundary angles are determined by Eqs. (43) and (44): $\varphi_0 = 0.3958$ rad $= 22.68°$, $\eta_0 = 0.6165$ rad $= 35.32°$. The total discontinuity angle is $\gamma_0 = 1.0123$ rad $= 58°$. Standing waves determined for the parameters given above and Eq. (69) are shown in Figure 9. The wave amplitude at the trailing contact edge according to Eq. (69) is $A_{sw} = R\gamma_0/\beta = 0.0076$ m, that is, $A_{sw}/w_0 = 0.507$. The central angle of the wavelength is $\theta_{sw} = 360°/\beta = 45°$. The amplitude of the standing waves decreases as they approach the leading contact edge.
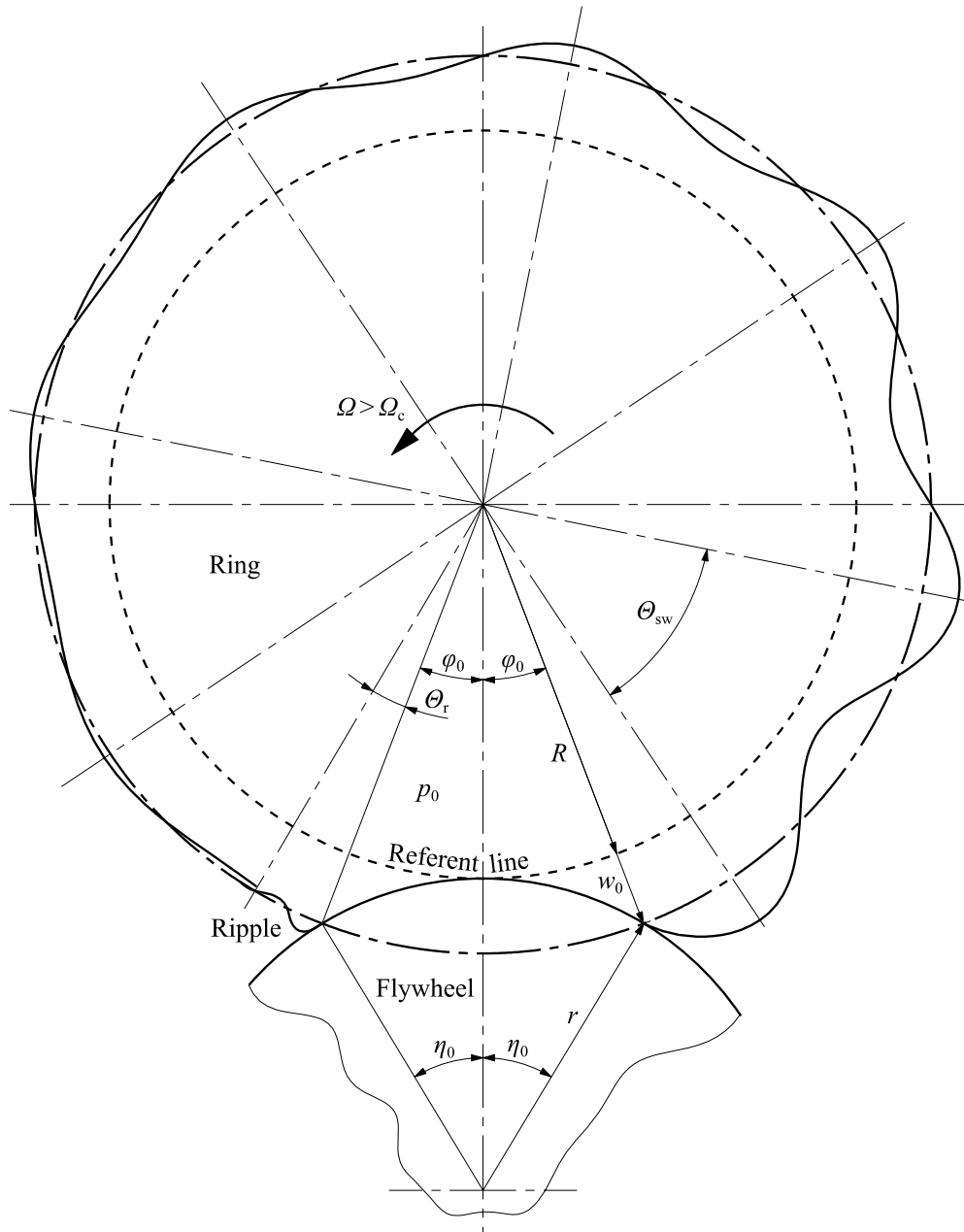
Fig. 9 *Ring standing waves and ripple, Ω_c = 320 rad/s, Ω = 400 rad/s*

Considering now the ripple at the leading contact edge, a very small value of the effective bending stiffness, $D = 1.41 \cdot 10^{-7}$ Nm², is used (assuming a large reduction of the modulus of elasticity at high deformation (curvature) due to the material non-linearity and balloon heating induced by the standing waves). The wave number, by employing Eq. (48), is $\lambda = 30$. The ripple amplitude according to Eq. (51) is $A_r = R\gamma_0/\lambda = 0.002$ m and the central angle of the wavelength is $\theta_r = 360°/\lambda = 12°$. The ripple is shown in Figure 9. It disappears after the first wave due to the strong decay coefficient equal to the wave number λ.

The internal radial load due to the flywheel penetration into the rotating ring, q_b, is determined according to Eqs. (54) and (57), and is shown in Figure 10, having a maximum value of 409 N/m. Furthermore, one finds for the bearing reaction forces, by employing Eq. (62), $F = 17$ N.

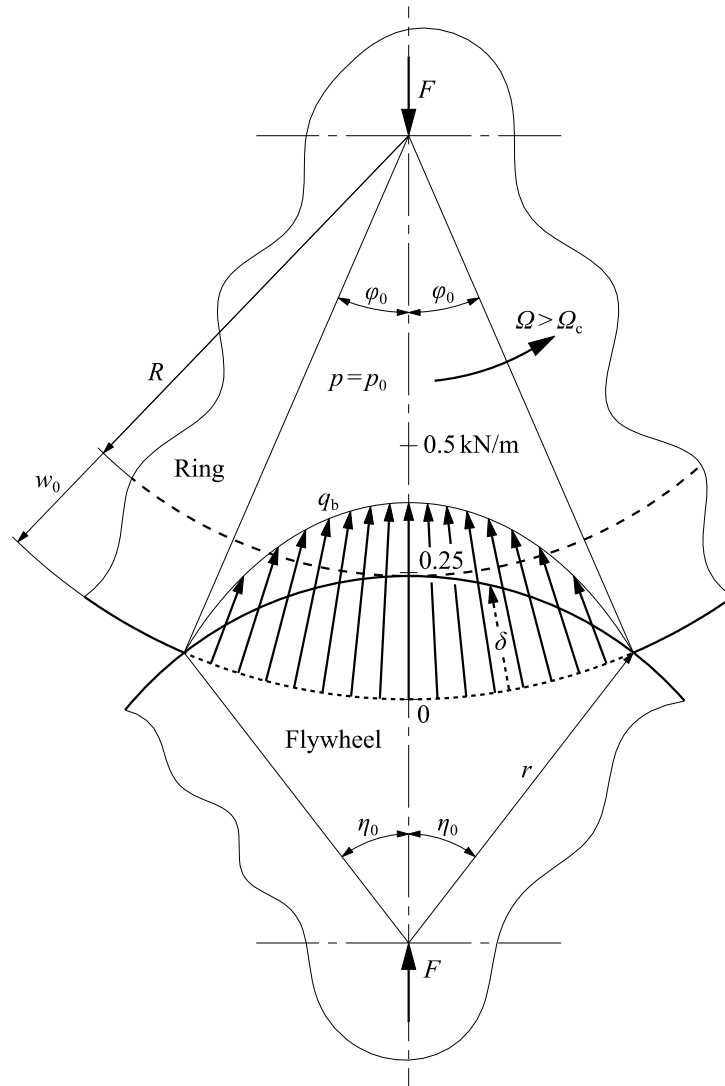**Fig. 10** *Radial internal load due to flywheel penetration in the rotating ring, Ω = 400 rad/s*

11. EVALUATION OF THE MATHEMATICAL MODEL

The ring is a rather simple model of the toroidal balloon of complex geometry and non-linear material, which behaves as a membrane exposed to very large deformations. In spite of this, a qualitative correlation analysis between the calculated ring response to the centrifugal load and video-recorded balloon behaviour is possible.

The results obtained during the experiment are elaborated in detail in [7]. The analysis includes photographs and diagrams of the relevant response parameters. Perhaps the most interesting one is the perspective view of the development of standing waves for the inflation pressure $p_0 = 15.5\,\text{kN/m}^2$. They are presented as a family of functions dependent on the position angle and the balloon angular velocity. For the purpose of the correlation analysis, the standing waves profile for the balloon angular velocity of 420 rad/s is shown in Figure 11. It is extracted from the perspective view and shown in a plane of an orthogonal coordinate system. The contact region of the balloon and the flywheel is indicated. The envelopes of the wave amplitudes are not smooth lines and the wavelengths are somewhat different.
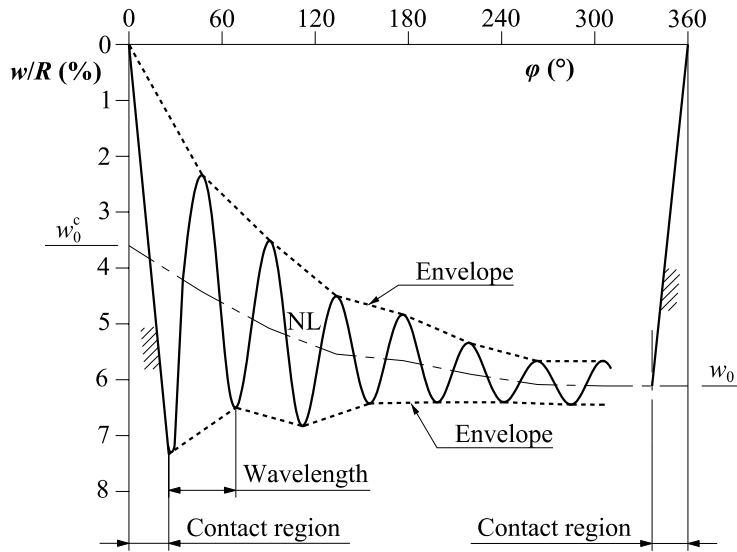
Fig. 11 *Recorded standing waves of a balloon tyre, Ω = 420 rad/s = 67 Hz, according to [7]*

Figure 12 shows the progress of the standing waves contact region w_{cr}/R with increasing angular velocity. The critical velocity of Ω_c = 282 rad/s, at which the development of standing waves is initiated, is indicated in the Figure. The increase in the central angle of the first wavelength, θ_{sw}, is also presented.
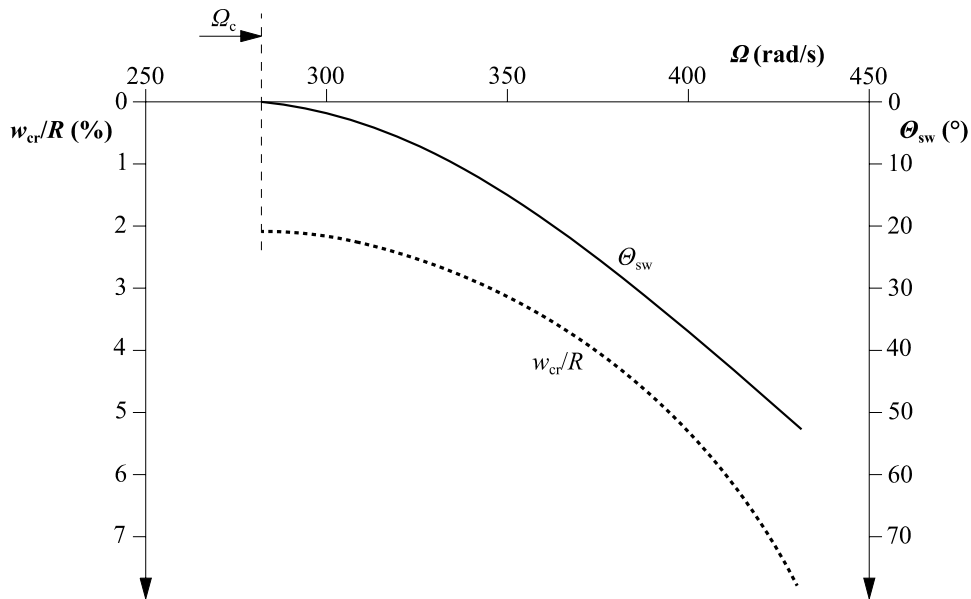
Fig. 12 *Recorded development of balloon and flywheel contact region in a radial direction, w_{cr}/R, and the central angle of the first standing wave, Θ_{sw}, according to [7]*

The calculated standing waves profile shown in Figure 9 is presented in Figure 13 in the same manner as the recorded profile in Figure 11. All characteristic central angles are included. The contact region is designated as well as the ripple on the leading contact edge. The calculated standing waves manifest almost all the characteristics of the recorded standing waves, Figures 13 and 11, respectively. There is a difference in the waves' neutral line NL. In reality, this line is a curve, while in the calculated waves profile it is a straight line. It seems that in the former case, this curve starts at the level of the balloon membrane radial displacement caused by the

critical rotation speed, w_0^c, and converges to the membrane radial displacement due to testing speed, w_0. These radial displacements are indicated in Figures 11 and 13.
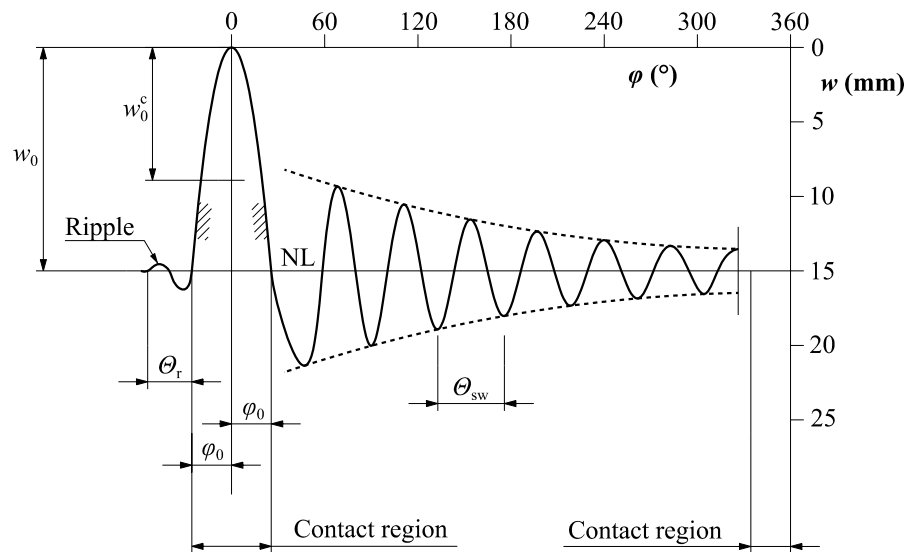

Fig. 13 *Calculated ring standing waves, Ω = 400 rad/s = 63.7 Hz*

In Figure 14, the recorded standing waves profile in the vicinity of the contact edges is shown. The kink at the leading contact edge is captured by the calculated ripple, Figure 9. However, with the present application of the standing waves theory, it is not possible to simulate the recorded standing waves profile at the trailing contact edge, Figures 9 and 14. The imperfection of the present solution concerning the deviation of the standing waves neutral line, Figure 11, and the disagreement of the standing waves profile at the trailing contact edge is analysed and overcome in the next section.
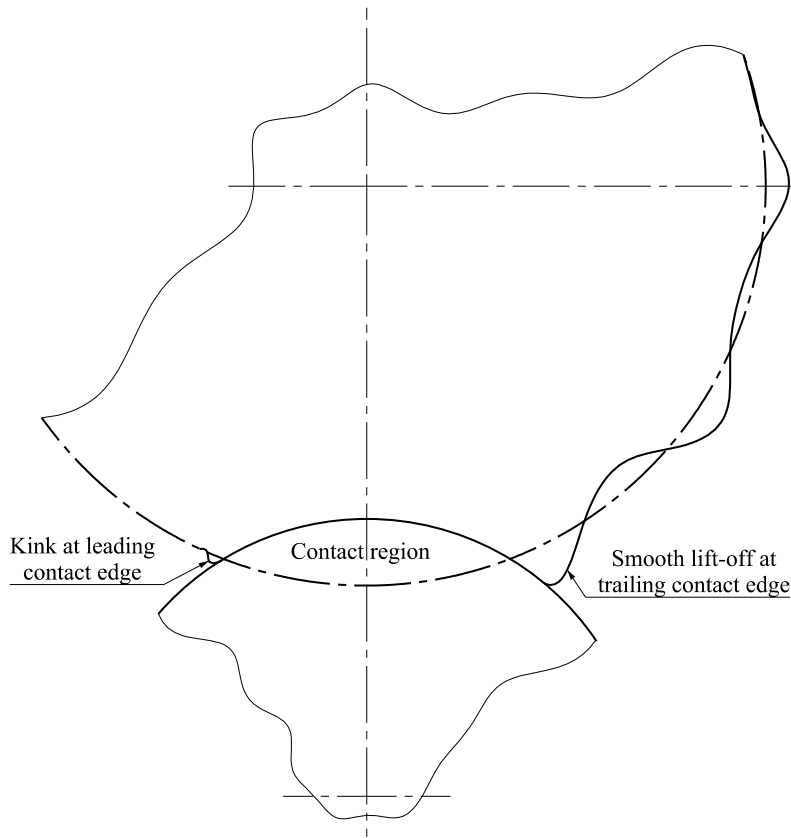
Fig. 14 *Lower portion of the balloon profile extracted from video data, $\Omega = 420\,rad/s = 67\,Hz$, according to [7]*

The critical rotation speed is a very important parameter in the dynamic behaviour of tyres. A diagram of critical speeds for the ring model calculated according to Eq. (71) is shown in Figure 15 as a function of the initial inflation pressure. On the other hand, the experimentally determined critical speeds as a function of the initial inflation pressure are shown in Figure 16. By comparing Figures 15 and 16, one can notice that the calculated critical speed is almost linear, while the recorded speed is parabolic. This is a result of the non-linearity of the problem, which is linearized in the present mathematical model.
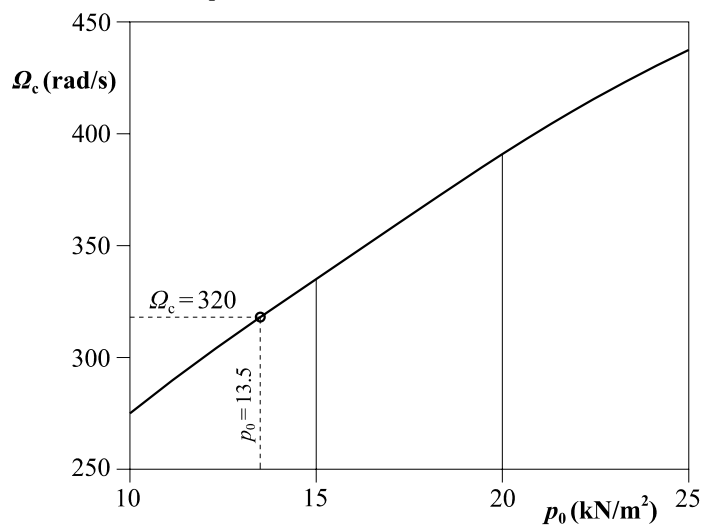
Fig. 15 *Calculated critical speed of the ring as a function of the initial inflation pressure*
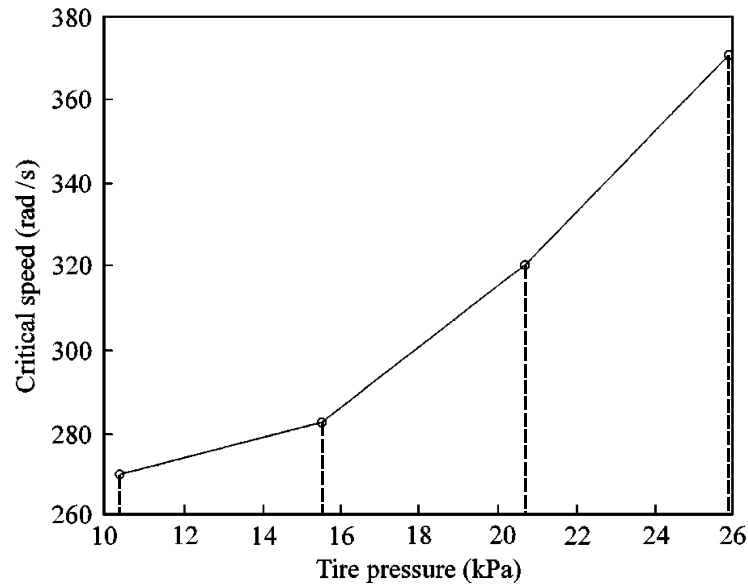
Fig. 16 *Recorded critical speed of the balloon as a function of the initial inflation pressure, adapted from [7]*

Within the evaluation of the mathematical model, it is worth mentioning that the predicted negligible small circumferential displacement agrees with the very small deviation of the marked radial lines on the balloon shell, [7].

12. IMPROVEMENT OF THE MATHEMATICAL MODEL

As elaborated in Section 9, by increasing the rotation speed, the resulting membrane force becomes compressive, and the ring relaxes and starts to behave like a whip. As a result, standing waves are generated, starting from point C related to the membrane radial displacement, w_0^C, Figure 17. For higher rotation speed, the membrane radial displacement is increased, w_0, Figure 17. Based on the experimental results, it is clear that the standing waves start at the contact edge, point P in Figure 17, with maximum amplitude, $w_0 - w_0^C$. This fact is a result of very small bending resistance due to the small bending stiffness. Hence, the discontinuity angle, γ_0, is mostly compensated by ripple, Figure 17. Another interesting phenomenon noticed in the analysis of the experimental results is a deviation of the neutral line of the standing waves. It starts at w_0^C, point C in Figure 17, and converges to the circle of w_0.
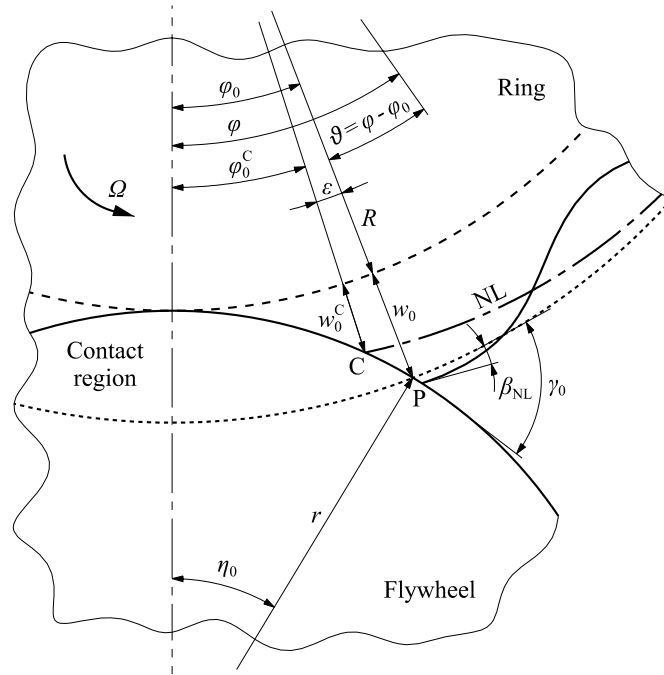
Fig. 17 *Boundary conditions according to experimental results*

The previously used boundary conditions in Section 5 are actually relevant for a ring with ordinary bending stiffness. In the case of a membrane ring, appropriate boundary conditions, according to the above explanation based on the experimental results, have to be given. In order to capture the variable neutral line of the standing waves, the homogeneous solution of differential equations with both trigonometric and exponential functions has to be employed, Eqs. (23) and (24). According to Eq. (31) one can write for the radial displacement with decreasing neutral line:

$$w = A_2\, e^{-\alpha \vartheta} + A_4\, sin\big(\beta \vartheta\big) + A_3\, cos\big(\beta \vartheta\big) + w_0 \tag{72}$$

Boundary conditions are specified according to Figure 17. The radial displacement at the flywheel contour, evident in Figure 17, is fulfilled by setting:

$$A_2 = -\Big(w_0 - w_0^C\Big)e^{-\alpha \varepsilon}$$
$$A_3 = w_0 - w_0^C, \tag{73}$$

where $\varepsilon = \varphi_0 - \varphi_0^C$. Substituting Eqs. (73) into (72) and incorporating damping, one obtains

$$w = \Big(w_0 - w_0^C\Big)\bigg[e^{-\mu \vartheta}\, cos\big(\beta \vartheta\big) - e^{-\alpha\big(\vartheta+\varepsilon\big)} \bigg] + w_0. \tag{74}$$

The values of some parameters involved in Eq. (74) were determined previously in Section 10: w_0^C = 0.0088 m, w_0 = 0.015 m. Parameters α and β are determined using Eqs. (18) and (19). In order to obtain the previously chosen wave number in Section 10, β = 8, the inflation pressure of 19.3 kN/m² is prescribed. In this case, one obtains α = 1.178. In addition, according to Eqs. (44), φ_0^C = 0.3273 rad and ε = 0.0685 rad. The standing waves of the membrane ring with the variable neutral line and ripples at the contact edges are shown in Figure 18. The ripples are determined according to the theory presented in Section 6. The continuity angle at the leading contact edge is γ_0, while at the trailing contact edge it is $\gamma^* = \gamma_0 - \beta_{NL}$, where β_{NL} is the rotation

of the neutral line. The calculated standing waves profile, Figure 18, agrees very well with the video-recorded one, Figure 14. By comparing Figure 19 and Figure 11, it is clear that the deviation of the neutral line is captured successfully by the improved mathematical model.
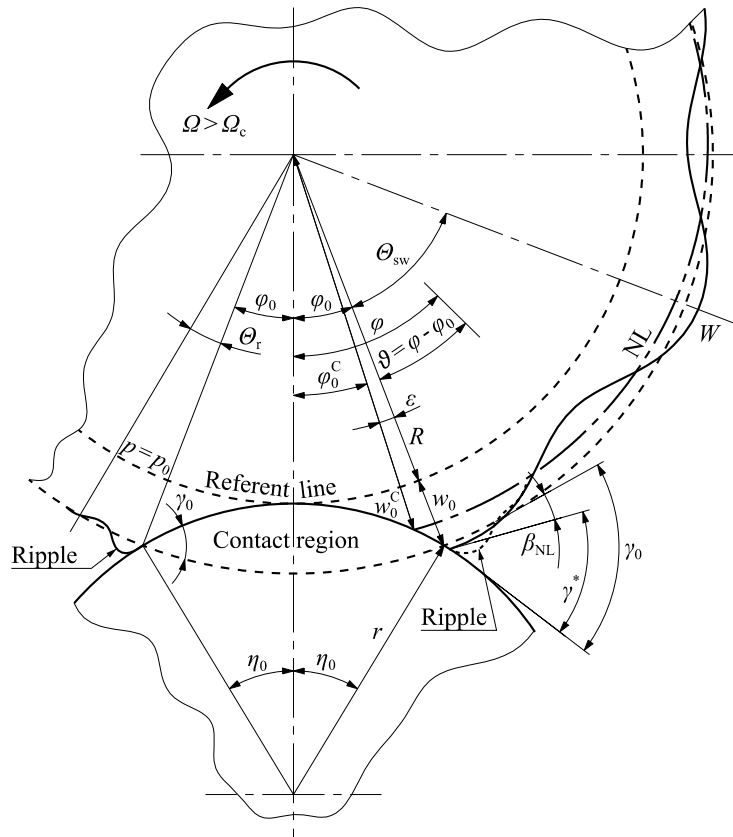
Fig. 18 *Smoothing of standing waves at contact edges, boundary conditions according to experimental results, $\Omega = 400$ rad/s*
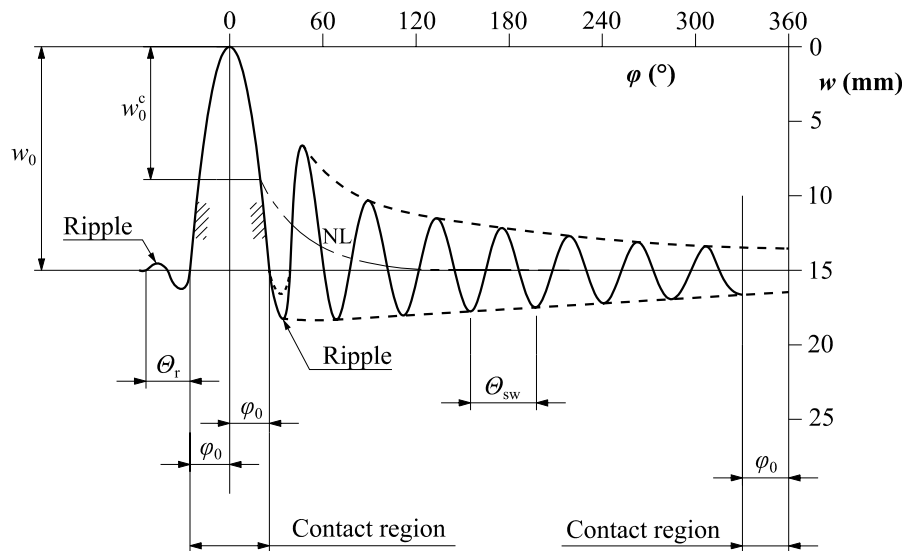
Fig. 19 *Calculated ring standing waves, boundary conditions according to experimental results, $\Omega = 400$ rad/s*

13. DISCUSSION

The mathematical model for the simulation of tyre standing waves, proposed in this paper by a relatively simple ring approximation, may be considered quite sophisticated when compared to the model presented in [7]. The latter model is developed for a theoretical interpretation of the experimental data recorded on a toroidal balloon tyre. However, the accompanying mathematical model from [7] is not as fruitful as the experimental study. It seems to be rather controversial and complicated, and requires a numerical solution, [30]. The advantage of the present mathematical model can be emphasized through several aspects.

First of all, in the mathematical model presented in [7], a balloon tyre is modelled as a ring with shear stiffness that does not comply with an essential membrane structure. Shear stiffness is normally attributable to thick structural elements like beams, plates and shells [34-36]. The balloon is exposed to very large membrane deformation and its circumferential generatrix behaves like a string on an elastic foundation. When the rotation speed is higher than the critical speed, a tensional mode turns into a deflection mode, in which the inflation pressure-induced geometric stiffness becomes activated. The inflation pressure is not considered in the standing waves theory in [7].

Furthermore, in the mathematical model presented in [7], it is assumed for simplicity that the ring is in contact with flat ground. The formulation of boundary conditions for standing waves as a non-linear contact problem of a tyre rolling on the ground makes that theory very complicated. In the actual set-up with a flywheel formulation, the contact problem in the present mathematical model is linear, and the relevant boundary conditions are determined in a relatively simple way. As a result, the standing waves are described explicitly by a decayed exponential function and a damped trigonometric function.

A special remark can be directed to the simulation of ripple at the leading contact edge presented in [7]. Ripple is a local bending boundary problem by which deflection discontinuity at the ring contact edge is overcome. In [7], the ripple and the standing waves are analysed as coupled problems. In order to capture the expected harmonic response, "shear damping" is introduced. Hence, both the ripple wavelength and its amplitude decay strongly depend on the rotation speed and damping. This might be a questionable approach, which is elaborated below.

In the present mathematical model, different orders of magnitude of standing waves and ripple are recognized. Therefore, this problem is decomposed into two separate tasks following the perturbation method. Ordinary differential equations of vibration of the ring on elastic support are formulated. The ripple wavelength is quite short and the decay coefficient is very large so that the ripple disappears almost within the first wavelength. The amplitude of the ripple strongly depends only on the ring rotation speed via the centrifugal load. Since the ripple is initiated as a static problem, it appears at both ring contact edges with almost the same magnitude.

Concerning the well-known resonance approach for the analysis of standing waves, this approach is based on the inherent circular periodicity of the tyre. However, several aspects of this approach do not conform naturally to the experimental observations. Indeed, if damping is not taken into account, then an increase in the rotation speed above the critical value would result in discrete changes in the shape of the standing waves. In the shock approach, the magnitude of the shock has no effect on the size or shape of the standing waves. In spite of the

fact that shock appears at approximately the same critical speed, it does not cause the standing waves.

14. CONCLUSION

The governing differential equations of motion for the analysis of ring standing waves are deduced from the cylindrical shell theory. Both radial and circumferential displacements are taken into account. Since the latter is much smaller than the former, it is neglected in the simplified standing waves theory. The undertaken analysis shows that both the sophisticated and simplified mathematical models give the same ring critical rotation speed. The coupling between radial and circumferential displacements enables capturing the recorded deviation of the standing waves neutral line.

In the new mathematical model presented in this paper, it is shown that the critical rotation speed strongly depends on the tyre inflation pressure. Standing waves arise from tyre instability when the moving-mass-induced membrane force overcomes the inflation pressure force. This agrees with the experimental data and one can conclude that the doubts concerning the application of the well-known resonant approach and the shock at the leading contact edge are overcome.

Based on the above facts, the proposed mathematical model for the simulation of standing waves is a step forward in successfully solving this challenging problem. The analytical presentation with relatively simple formulae enables the influence of each parameter involved in the response to be recognized. Since the mathematical model is evaluated qualitatively and improved by comparing the calculated results with the data recorded while performing a very sophisticated experiment, it can be used as a milestone for further similar investigations of tyre standing waves.

As a next step, standing waves in ordinary car and truck tyres on a test bed over a drum or on the ground can be investigated using the same approach. In this case, complete differential equations of vibrations with bending stiffness have to be used. In the governing equations, shear stiffness can also be incorporated. Boundary conditions are different from those specified for a membrane ring. As a result, ripples at the contact edges will not be as pronounced as in the case of a balloon tyre. The reliable determination of bearing reaction forces, presented in the new theory of the generation of standing waves, is quite important for the bearing design.

15. ACKNOWLEDGEMENT

16. REFERENCES

[1]   W.F. Ames, Waves in tires: Part I: Literature review on traveling waves, *Text. Res. J.* 40(6) (1970) 498-503. https://doi.org/10.1177/004051757004000602

[2]   S.C. Huang, W. Soedel, Response of rotating rings to harmonic and periodic loading and comparison with the inverted problem, *J. Sound Vib.* 118(2) (1987) 253-270.

https://doi.org/10.1016/0022-460X(87)90524-4

[3]   S.C. Huang, The vibration of rolling tyres in ground contact, *Int. J. Vehicle Design* 13(1) (1992) 78-95.

[4]   S.C. Huang, C.K. Su, In-plane dynamics of tires on the road based on an experimentally verified rolling ring model, *Vehicle Syst. Dyn.* 21(1) (1992) 247-267.

https://doi.org/10.1080/00423119208969011

[5]   D.S. Stutts, W. Soedel, A simplified dynamic model of the effect of internal damping on the rolling resistance in pneumatic tires, *J. Sound Vib.* 155(1) (1992) 153-164.

https://doi.org/10.1016/0022-460X(92)90652-E

[6]   N.J. Lindsley, J.P. Cusumano, Critical Speed Analysis of a non-linear strain ring dynamical model for aircraft tires, *SAE Techn. Paper* (1993) 932580.

https://doi.org/10.4271/932580

[7]   A. Chatterjee, J.P. Cusumano, J.D., Zolock, On contact-induced standing waves in rotating tires: Experiment and theory, *J. Sound Vib.* 227(5) (1999) 1049-1081.

https://doi.org/10.1006/jsvi.1999.2395

[8]   L.E. Kung, W. Soedel, T.Y. Yang, Free vibration of a pneumatic tire-wheel unit using a ring on an elastic foundation and a finite element model, *J. Sound Vib.* 107(2) (1986) 181-194. https://doi.org/10.1016/0022-460X(86)90231-2

[9]   X.W. Ji, Y.M., Gao, X.D., Qiu, Y.D., Li, J.D., Zhuang, J.D., The dynamic stiffness and damping characteristics of the tire, *Automot. Eng.* 16(5) (1994) 315-320.

[10]   Y.P. Chang, M. El-Gindy, D.A. Streit, Influence of tyre loading and inflation pressure on standing waves phenomenon using PAM-SHOCK, *Int. J. Heavy Vehicle Syst.* 10(1/2) (2003) 86-111. https://doi.org/10.1504/IJHVS.2003.002436

[11]   E. Vinesse, H. Nicollet, Surface waves on the rotating tyre: An application of functional analysis, *J. Sound Vib.* 126(1) (1988) 85-96.

https://doi.org/10.1016/0022-460X(88)90400-2

[12]   C. Lecomte, W.R. Graham, M. Dale, A shell model for tyre belt vibrations, *J. Sound Vibr.* 329(10) (2010) 1717–1742. https://doi.org/10.1016/j.jsv.2009.11.022

[13]   W. Soedel, On the dynamic response of rolling tires according to thin shell approximations, *J. Sound Vib.* 41(2) (1975) 233-246.

https://doi.org/10.1016/S0022-460X(75)80099-X

[14]   J. Padovan, On viscoelasticity and standing waves in tires, *Tire Sci. Techn.* 4(4) (1976) 233-246. https://doi.org/10.2346/1.2167224

[15]   J. Padovan, On standing waves in tires, *Tire Sci. Techn.* 5(2) (1977) 83-101.

https://doi.org/10.2346/1.2167234

[16]   R. Kennedy, J. Padovan, Finite element analysis of a steady-state rotating tire subjected to point load or ground contact, *Tire Sci. Techn.* 15(4) (1987) 243-260.

https://doi.org/10.2346/1.2148792

[17]   J. Padovan, A. Kazempour, F. Tabaddor, B. Brockman, Evaluation of critical speeds in high speed aircraft tires, *SAE Techn. Paper* (1989) 892349.

https://doi.org/10.4271/892349

[18] R.A. Brockman, J.H. Champion, J.P. Medzorian, Finite element analysis of tire critical speeds, *Comput. Struct.* 43(3) (1992) 581-593.

https://doi.org/10.1016/0045-7949(92)90290-G

[19] J.R. Cho, K.W. Kim, H.S. Jeong, Numerical investigation of tire standing wave using 3-D patterned tire model, *J. Sound Vib.* 305(4–5) (2007) 795-807.

https://doi.org/10.1016/j.jsv.2007.04.049

[20] S. Ozaki, W. Kondo, Finite element analysis of tire traveling performance using anisotropic frictional interaction model, *J. Terramech.* 64 (2016) 1-9.

https://doi.org/10.1016/j.jterra.2015.12.001

[21] B. Mashadi, S. Ebrahimi-Nejad, M. Abbaspour, A rolling resistance estimate using nonlinear finite element numerical analysis of a full three-dimensional tyre model, *Proc. Inst. Mech. Eng., Part D: J. Autom. Eng.* 233(1) (2019) 147-160.

https://doi.org/10.1177/0954407018802733

[22] S.T. Zhou, M. Du, P.F. Sun, Y.J. Chiu, J.W. Fan, Experimental and theoretical analysis of high-speed radial tire standing waves, *J. Brazilian Soc. Mech. Sci. Eng.* 42 (2020) 200.

https://doi.org/10.1007/s40430-020-2253-2

[23] G.R. Potts, C.A. Bell, L.T. Charek, T.K. Roy, Tire vibrations, *Tire Sci. Techn.* 5(4) (1977) 202-225. https://doi.org/10.2346/1.2167240

[24] M. Hirano, T. Akasaka, Natural Frequencies of the bias tire, *Tire Sci. Techn.* 4(2) (1976) 86-114. https://doi.org/10.2346/1.2167218

[25] L.E. Kung, Radial vibrations of pneumatic radial tires, *SAE Techn. Paper* (1990) 900759.

https://doi.org/10.4271/900759

[26] R.W. Scavuzzo, T.R. Richards, L.T. Charek, Tire vibration modes and effects on vehicle ride quality, *Tire Sci. Techn.* 21(1) (1993) 23-39.

https://doi.org/10.2346/1.2139520

[27] C. Gonzalez Diaz, P. Kindt, J. Middelberg, S. Vercammen, C. Thiry, R. Close, J. Leyssens, Dynamic behaviour of a rolling tyre: Experimental and numerical analyses, *J. Sound Vib.* 364 (2016) 147-164. https://doi.org/10.1016/j.jsv.2015.11.025

[28] R.N. Dodge, The dynamic stiffness of a pneumatic tire model, *SAE Techn. Paper* (1965) 650491. https://doi.org/10.4271/650491

[29] P.M. Wagner, Initial critical speed laboratory tests of three aircraft bias ply tires, WRDCTM-89-194-FIVMA, U.S. Force, 1989.

[30] V.V. Krylov, O. Gilbert, On the theory of standing waves in tyres at high vehicle speeds, *J. Sound Vib.* 329(21) (2010) 4398-4408.

https://doi.org/10.1016/j.jsv.2010.05.001

[31] N. Alujević, N. Campillo-Davo, P. Kindt, W. Desmet, B. Pluymers, S. Vercammen, Analytical solution for free vibrations of rotating cylindrical shells having free boundary conditions, *Engineering Structures* 132 (2017) 152-171.

https://doi.org/10.1016/j.engstruct.2016.11.008

[32] I. Senjanović, I. Ćatipović, N. Alujević, N. Vladimir, D. Čakmak, A finite strip for the vibration analysis of rotating cylindrical shells, *Thin-Wall. Struct.* 122 (2018) 158-172.

https://doi.org/10.1016/j.tws.2017.10.017

[33] I. Senjanović, D. Čakmak, N. Alujević, I. Ćatipović, N. Vladimir, N., D.S. Cho, Pressure and rotation induced tensional forces of toroidal shell and their influence on natural vibrations, *Mech. Res. Comm.* 96 (2019) 1-6.

https://doi.org/10.1016/j.mechrescom.2019.02.003

[34] I. Senjanović, N. Vladimir, N. Hadžić, M. Tomić, New first order shear deformation beam theory with in-plane shear influence, *Eng. Struct.* 110 (2016) 169-183.

https://doi.org/10.1016/j.engstruct.2015.11.032

[35] I. Senjanović, N. Vladimir, M. Tomić, An advanced theory of moderately thick plate vibrations, *J. Sound Vib.* 332(7) (2013) 1868-1880.

https://doi.org/10.1016/j.jsv.2012.11.022

[36] M. Endo, An alternative first-order shear deformation concept and its application to beam, plate and cylindrical shell models, *Compos. Struct.* 146 (2016) 50-61.

https://doi.org/10.1016/j.compstruct.2016.03.002